Dual-Source Evaporation of Silver Bismuth Iodide Films for Planar Junction Solar Cells

Journal:	*Journal of Materials Chemistry A*
Manuscript ID	TA-ART-09-2018-008679.R2
Article Type:	Paper
Date Submitted by the Author:	23-Dec-2018
Complete List of Authors:	Khazaee, Maryam; Duke University, Mechanical Engineering and Materials Science Sardashti, Kasra; Duke University, Mechanical Engineering and Materials Science Chung, Ching-Chang; North Carolina State University, Department of Materials Science and Engineering Sun, Jon-Paul; Duke University, Mechanical Engineering and Materials Science Zhou, Hanhan; North Carolina State University, Department of Materials Science and Engineering Bergmann, Eric; Dalhousie University, Physics and Atmospheric Science Dunlap-Shohl, Wiley; Duke University, Mechanical Engineering and Materials Science Han, Qiwei; Department of Chemistry, Duke University Hill, Ian G.; Dalhousie University, Physics and Atmospheric Science Jones, Jacob; North Carolina State University, Department of Materials Science and Engineering Lupascu, Doru; Universität Duisburg-Essen, Institute for Materials Science Mitzi, David; Duke University, Mechanical Engineering and Materials Science

SCHOLARONE™
Manuscripts

Dual-Source Evaporation of Silver Bismuth Iodide Films for Planar Junction Solar Cells

Maryam Khazaee,[ab] Kasra Sardashti,[a] Ching-Chang Chung,[c] Jon-Paul Sun,[ad] Hanhan Zhou,[c] Eric Bergmann,[d] Wiley A. Dunlap-Shohl,[a] Qiwei Han,[ae] Ian G. Hill,[d] Jacob L. Jones,[c] Doru C. Lupascu,[b] and David B. Mitzi[*ae]

[a] Department of Mechanical Engineering and Materials Science, Duke University, Durham, North Carolina 27708, United States
[b] Institute for Materials Science and Center for Nanointegration Duisburg-Essen (CENIDE), University of Duisburg-Essen, Universitätsstraße 15, 45141 Essen, Germany
[c] Department of Materials Science and Engineering, North Carolina State University, Raleigh, North Carolina 27695, United States
[d] Department of Physics and Atmospheric Science, Dalhousie University, Halifax, Nova Scotia B3H 3J5, Canada
[e] Department of Chemistry, Duke University, Durham, North Carolina 27708, United States
*E-mail: david.mitzi@duke.edu

Non-toxic and air-stable silver bismuth iodide semiconductors are promising light absorber candidates for photovoltaic applications owing to a suitable band gap for multi- or single-junction solar cells. Recently, solution-based film fabrication approaches for several silver bismuth iodide stoichiometries have been investigated. The current work reports on a facile and reproducible two-step coevaporation/annealing approach to deposit compact and pinhole-free films of $AgBi_2I_7$, $AgBiI_4$ and Ag_2BiI_5. X-ray diffraction (XRD) in combination with scanning electron microscopy (SEM)/energy-dispersive X-ray spectroscopy (EDX) analysis reveal formation of pure cubic ($Fd\bar{3}m$) phase $AgBi_2I_7$, cubic ($Fd\bar{3}m$) or rhombohedra ($R\bar{3}m$) phase $AgBiI_4$, each with > 3 µm average grain size, or the rhombohedral phase ($R\bar{3}m$) Ag_2BiI_5 with > 200 nm average grain size. A phase transition from rhombohedral to cubic structure is investigated via temperature-dependent X-ray diffraction (TD-XRD). Planar-junction photovoltaic (PV) devices are prepared based on the coevaporated rhombohedral $AgBiI_4$ films, with titanium dioxide (TiO_2) and poly(3-hexylthiophene) (P3HT) as electron- and hole-transport layers, respectively. The best-performing device exhibited a power conversion efficiency (PCE) of as high as 0.9% with open-circuit voltage (V_{OC}) > 0.8 V in the reverse scan direction (with significant hysteresis).

Introduction

Semiconductor lead-halide perovskites serve as high-performance absorber materials for thin-film solar cells, owing to their remarkable optical, electrical and chemical properties.[1-7] Ease of solution-based processing coupled with inexpensive and earth-abundant constituents is expected to reduce production costs relative to commercial solar cells – e.g., silicon, CdTe, $Cu(In,Ga)(S,Se)_2$ (CIGS) and GaAs.[8] Despite the intense advancement in PCE of lead-halide perovskite solar cells (23.7%),[9] environmental toxicity of Pb and low stability under ambient conditions remain two key issues hindering large-scale commercialization of this technology.[10-13] The three-dimensional (3D) perovskite network with general formula ABX_3 (A = $CH_3NH_3^+$, $NH_2CHNH_2^+$, Cs^+ and Rb^+; B = Pb^2; X = Cl^-, Br^- and I^-) plays a key role in generating the outstanding properties and consists of corner-sharing $[BX_6]$ octahedra infiltrated by either an organic or inorganic monovalent cation A^+. Although incorporation of inorganic A^+ cations in place of the organic analogues has enhanced the stability of resulting devices,[14,15] the demanded level of stability for large-scale commercialization still remains to be achieved. Tin and germanium (Sn^{2+}, Ge^{2+}) have been independently considered for the "B" site (to remove Pb), but are environmentally unstable owing to the propensity of these elements to oxidize to the 4+ valence state (Sn^{4+} and Ge^{+4}).[16-20] Recently, mixtures of Sn^{2+} and Ge^{2+} have been proposed to lead to moderate performance levels (up to 6.90%) and improved stability.[21-23]

Alternatively, lead-free light harvester materials can be realized by substituting Sn^{2+} with isoelectronic Sb^{3+}, with a typical formula $A_3Sb_2X_9$ (A = CH_3NH_3, K, Rb, Cs; X = Cl, Br, I).[18,24-27] Despite low reported PCE of 0.08% for the $(CH_3NH_3)_3Sb_2I_9$ solar cell,[26] Zhou et al. has reported that chlorine incorporation promotes formation of the 2D layered structure $(CH_3NH_3)_3Sb_2I_9$, yielding a PCE of over 2%.[28] Recently, the efficiency of $(CH_3NH_3)_3Sb_2I_9$ solar cells has reached up to 2.77% via controlling the crystallinity of the fabricated films through a combination of antisolvent treatment and insertion of a hydrophobic interlayer.[25] Moreover, a recent report by Buonassisi et al. suggests that the highest PCE of 0.76% for $Rb_3Sb_2I_9$ compared to the relatively poor PV performances of $K_3Sb_2I_9$ (0.17%) and $Cs_3Sb_2I_9$ (0.03%) originates from the large exciton binding energies and large carrier effective masses, especially in the latter materials.[24] Low-toxicity and stable Bi^{3+} represents another candidate to replace Pb, offering similar ionic radius and identical electronic structure to Pb^{2+}. However, direct incorporation of Bi is complicated (as for Sb) by its trivalent oxidation state (vs. divalent for Pb), as charge balance requirements induce structural changes to the perovskite lattice that substantially alter material properties when substituted for Pb (unless balanced by an equal amount of a monovalent cation, such as Ag^+). Recently, several semiconductor Bi-based halides, including "defect perovskites" $A_3Bi_2I_9$ (A = CH_3NH_3, NH_4, K, Rb, Cs),[29-35] "double perovskites" Cs_2AgBiX_6 (X = Br, Cl),[36,37] $CuBiI_4$[38,39] and several stoichiometries of silver bismuth iodide (e.g. $AgBiI_4$, $AgBi_2I_7$, Ag_3BiI_6),[40-42] have been investigated as potential absorber materials for thin film solar cells. Among them, the silver bismuth iodides have the most suitable band gap (1.7-1.8 eV) for single junction devices.[40,42,43]

Silver bismuth iodide structures with general formula of $Ag_xBi_yI_z$, where z = x + 3y, consist of the formally monovalent Ag^+ cation, trivalent Bi^{+3} cation and monovalent I^- anion, in which $[AgI_6]$ and $[BiI_6]$ octahedra share edges. The cationic sublattice of these compounds involves disorder due to the partial occupancy of a single position by silver, bismuth or their respective vacancies, permitting the wide range of stoichiometries observed in literature. The edge-sharing octahedra arrange either in a rhombohedral $CdCl_2$ layer-type structure, in which every other (111) plane is occupied with Ag^+ or Bi^{+3}, or a closely-related 3D-network defect-spinel cubic structure with vacant tetrahedral sites (**Fig. 1e** and **f**). Formation of each of these structures in a Ag-Bi-I compound evidently depends on several parameters including composition, annealing conditions and preparation methods. Among the $Ag_xBi_yI_{x+3y}$ compounds, Sargent and co-workers reported on thin film fabrication of cubic $AgBi_2I_7$ and proposed a crystal structure similar to $ThZr_2H_7$, in which both $[AgI_6]$ octahedra and $[BiI_8]$ hexahedra coexist in the crystal structure.[40] However, Yan and co-workers argued that $AgBi_2I_7$ adopts a Ag-deficient $AgBiI_4$-type structure.[44] Further studies showed that Ag_3BiI_6 and $AgBiI_4$ are additional prospective ternary compounds in the AgI-BiI_3 phase diagram, in which Ag_3BiI_6 indexes to a rhombohedral unit cell (space group: $R\bar{3}m$) with a = 4.3537(6) Å, c = 20.810(4) Å and Z = 1, whereas $AgBiI_4$ crystalizes in the cubic space group $Fd\bar{3}m$ with a = 12.223(1) Å and Z = 8.[41,45] On the other hand, Rosseinsky et al. have reported both rhombohedral and cubic structures for $AgBiI_4$, depending on the synthesis approach employed for growing this nominal stoichiometry.[42] Although they have obtained a cubic structure (space group $Fd\bar{3}m$) with lattice parameters a = 12.2104(3) Å and a = 12.21446(4) Å, for $AgBiI_4$ synthesized by a solution-based process and in powder (bulk) form, respectively, single-crystal $AgBiI_4$ was indexed to a rhombohedral unit cell ($R\bar{3}m$) with a = 4.3187(1) Å and c = 20.6004(8) Å. On the basis of density functional theory (DFT) calculations, they have reported similar stability levels for the defect-spinel cubic and $CdCl_2$ layer-type structures. Another reported composition for the Ag-Bi-I system, Ag_2BiI_5, has the same crystal structure as Ag_3BiI_6 and crystallizes in the space group $R\bar{3}m$ with a = 4.350 Å and c = 20.820 Å.[46] Moreover, Aramaki and co-workers have reported that increasing Bi-content of the Ag-Bi-I compound from Ag_3BiI_6 to $AgBi_2I_7$ causes an increase in the number of vacant sites in the cation sublattice. They also have proposed three possible crystallographic structures for $AgBiI_4$ consisting of *R3m* (trigonal), *C2/m* (monoclinic), and *Fd3m* (cubic).[43] Oldag et al. reported an activation energy of 0.44 eV for Ag migration in $AgBiI_4$, which is similar to the activation energy of iodine migration of 0.48 eV in methylammonium lead iodide ($CH_3NH_3PbI_3$), suggesting facile migration of Ag in this system.[41,47]

Based on the above studies, it is apparent that not only the target composition of the compound but also the synthesis pathway can have substantial influence on the formation of the final crystal systems. In most of these studies, solution-based approaches have been applied to grow thin films of silver bismuth iodide. Photovoltaic performance of solar cells with a *mesoporous* architecture and solution-processed $AgBi_2I_7$, Ag_2BiI_5, Ag_3BiI_6, $Ag_2Bi_3I_{11}$ (cubic structure) and most recently $AgBiI_4$ as absorber materials, have been reported with efficiencies of 1.22,[40] 2.1[48] or 2.31[49] or 2.62,[50] 4.3,[43] 0.78,[51] and 2.2[50] or 2.1%,[52] respectively. To date, no report of the photovoltaic performance of vacuum-deposited silver bismuth iodide in a planar device structure has appeared in the literature. In the current study, a facile two-step deposition method consisting of coevaporation followed by post-deposition annealing is applied to fabricate polycrystalline films of silver bismuth iodide with various stoichiometries (e.g. $AgBi_2I_7$, $AgBiI_4$, and Ag_2BiI_5). Depending on the composition, the thin film morphology changes from smooth, pin-hole-free and coarse grain (> 3 μm diameter), to fine grain (< 100 nm diameter) with increased pinhole density. A comprehensive structural study reveals that a crystallographic phase transition from rhombohedral to cubic occurs in Bi-rich ternary compounds due to compositional and other thermally-induced changes in the film. In contrast, Ag-rich films dominantly remain in the rhombohedral phase, independent of annealing. The compositional characteristics of the films are studied by SEM/EDX. Moreover, the electronic properties of the optimized films are characterized by ultraviolet photoelectron spectroscopy (UPS) and inverse photoemission spectroscopy (IPES). PV devices with planar structure based on rhombohedral $AgBiI_4$ exhibit a power conversion efficiency of as high as 0.9 % (reverse scan direction), with open circuit voltage of > 0.8 V and a short circuit current density of ~2 mA/cm^2. Substantial hysteresis in the devices points to barriers to charge extraction or defects in the current device configuration.

Experimental

Thin Film Growth

Thin films of silver bismuth iodide (thickness ≈ 450 nm) were grown by a dual-source coevaporation approach using Radak sources in an Angstrom Engineering (EvoVac) thermal evaporator. The two Radak sources were filled with BiI_3 (99.999%, Alfa Aesar) and AgI (99.9%, Alfa Aesar) powders. To examine possible changes in the stoichiometry of the final films, various deposition rate ratios for the two precursors – i.e. r = rate (AgI)/rate(BiI_3) = 0.2, 0.6, 0.8, and 1.2– were tested. Note that the specific rate ratios used do not, in general, translate to the same elemental ratios in the final films, due to different volatilities, evaporation and sticking properties for the two metal halides. Nevertheless, there is the expectation that changes in "r" will correlate with changes in resulting film composition. The base pressure for the evaporation was below 2×10^{-6} Torr. During the deposition, no intentional substrate heating was applied. Post-deposition annealing of the films was performed inside a nitrogen-filled glovebox. For this purpose, an as-deposited film was placed under a quartz cover in preheated BiI_3 vapor for a specified period of time followed by quenching of the film to room temperature (r = 0.6, 0.8, 1.2). In addition, the as-deposited Bi-rich films (e.g. r = 0.2 and 0.6) were annealed at 180 °C for 15 min under N_2 without an excess of BiI_3 vapor. Annealing temperatures and times ranged over 150–200 °C and 10–30 min, respectively, for achieving single-phase and pinhole-free polycrystalline films. After testing various annealing conditions for the deposited films with different rate ratios, post-deposition annealing at 180 °C for 15 min (either with or without excess BiI_3 vapor) was determined to be the optimal condition to achieve smooth and pinhole-free films with relatively large grain size.

Thin Film Characterization

XRD measurements were performed using a PANalytical Empyrean X-ray diffractometer (Cu Kα radiation with operating voltage/current of 45 kV/40 mA) under ambient conditions with a 10–60° 2θ scattering angle range. Pawley refinement was conducted using the PANalytical HighScore Plus software to determine lattice parameters. Crystallographic phase transitions were investigated by TD-XRD measurements using an Empyrean X-ray diffractometer with an Anton Paar XRK 900 reactor chamber. A continuous N_2 flow with a flow rate of 20 ml/min was applied throughout the variable-temperature measurements. Surface morphology and film grain size were characterized using a FEI XL30 scanning electron microscope. Compositional measurements were carried out using EDX (FEI Verios 460L) with a beam current of 1.6 nA and beam voltage of 20 kV. Average film composition was characterized by collecting SEM/EDX spectra of three different areas of the deposited film. Thin films of AgI and BiI_3 were used as EDX standards. Optoelectronic properties of the films were studied using optical absorption spectroscopy (Shimadzu UV3600 spectrometer) on films deposited on soda-lime glass substrates. Photoelectron spectroscopy (PES) measurements, including X-ray photoelectron spectroscopy (XPS), UPS and IPES, were conducted under ultra-high vacuum (10^{-10} mbar) on thin films deposited on indium tin oxide (ITO)-coated glass substrates. The films were analyzed as-loaded to avoid any sputtering damage. For UPS and XPS studies, the analysis chamber was equipped with a hemispherical energy analyzer (Specs Phoibos 150). For XPS, Al Kα (1486.6 eV) and Mg Kα (1253.6 eV) sources were used. UPS measurements were carried out using a He I (hν = 21.22 eV) source. IPES measurements were performed in the isochromat mode using a homemade spectrometer located in the PES analysis chamber, with a resolution of approximately 0.6 eV as determined by the width of the Fermi edge of clean polycrystalline silver. The positions of the Fermi edge were used to align the UPS and IPES energy scales.

Device Fabrication and Characterization

TiO_2 solution was prepared by dissolving 2:1 (v/v) of titanium diisopropoxide bis(acetylacetonate) (75 wt. % in isopropanol, Sigma Aldrich) in ethyl alcohol (anhydrous, ≥99.5%, Sigma Aldrich). Spray pyrolysis was used to fabricate a thin (30–50 nm) layer of compact TiO_2 on fluorine-doped tin-oxide (FTO)-coated glass substrates (Kintec, sheet resistance = 10 Ω/sq, glass thickness = 2.2 mm). During the spray coating, the substrate temperature was maintained at 450 °C using a hot plate. Deposition was followed by annealing of the substrates at 500 °C for 1 h. The TiO_2-coated substrates were then transferred to the thermal evaporator (as described above), wherein a thin layer of silver bismuth iodide was deposited via coevaporation of AgI and BiI_3 with $r = 0.6$. Subsequently, post-deposition annealing was carried out in nitrogen atmosphere at 180 °C for 15 min followed by a slow-cooling process. The hole transport material, P3HT (Solaris), was dissolved to a concentration of 20 mg/ml in chlorobenzene (anhydrous, Sigma Aldrich) and the solution was deposited by spin-coating at 3000 rpm for 30 s on top of the annealed silver bismuth iodide films. Finally, 80 nm thick gold (Au) electrodes were deposited on top of the devices through a shadow mask by thermal evaporation at ~ 10^{-6} Torr base pressure.

Current density-voltage (J-V) characterization of the planar solar cells was performed using an Oriel solar simulator and a Keithley source meter under 1 sun AM 1.5G illumination, calibrated by a Si reference cell from Newport Corp. A mask with 0.1 cm^2 aperture area was utilized to define the active area for each cell. An EQE spectrum was recorded using an Enlitech QE–R instrument, in AC mode with chopper frequency of 165 Hz, in the absence of bias voltage or illumination. Calibration was carried out using a certified silicon solar cell by Enlitech Company.

Results and discussion

Phase purity and unit cell parameters of the films grown in the present study were examined by XRD and average compositions were characterized using SEM/EDX, as a function of component metal halide mixing ratio during coevaporation (r = rate(AgI)/rate(BiI_3); see the Experimental Section for more details). The obtained XRD pattern for the as-deposited film of $r = 0.2$ matches a rhombohedral unit cell ($R\bar{3}m$, no. 166) with lattice parameters $a = b = 4.3502(3)$ Å, $c = 20.693(2)$ Å (**Fig. 1a** left). Fitting the experimental XRD pattern for the annealed film of $r = 0.2$ (180 °C, 15 min under N_2) yields a two-phase mixture of rhombohedral ($R\bar{3}m$, no. 166) with $a = b = 4.3479(4)$ Å, $c = 20.641(2)$ Å and cubic ($Fd\bar{3}m$, no.227) with $a = b = c = 12.1944(4)$ Å (**Fig. 1a** right). BiI_3 impurity peaks are also observed for both as-deposited and annealed films, likely originating from the large amounts of BiI_3 applied during the coevaporation process. SEM/EDX measurements verify high average Bi content, yielding $Ag_{0.49}Bi_{2.13}I_{7.00}$ and $Ag_{0.72}Bi_{2.07}I_{7.00}$ for the as-deposited and annealed films, respectively. Given the mixed phase nature of the $r = 0.2$ films, they will not be further considered in this study.

The obtained XRD pattern for the $r = 0.6$ as-deposited film indexes to a rhombohedral unit cell with lattice parameters $a = b = 4.3546(1)$ Å, $c = 20.7430(3)$ Å in the $R\bar{3}m$ space group (**Fig. 1b** left). A crystallographic phase transition from rhombohedral to cubic structure occurs upon post-deposition annealing of the as-deposited film. This phase transition occurs regardless of whether the film is annealed under BiI_3 vapor (**Fig. 1b** right) or only under N_2 (**Fig. S1a**). The XRD pattern of the annealed film without BiI_3 yields a cubic structure ($Fd\bar{3}m$) with lattice parameters $a = b = c = 12.2079(2)$ Å, with little difference noted compared to films annealed under excess of BiI_3 vapor ($a = b = c = 12.2043(3)$ Å) and with previously published reports for the similar film compositions prepared via solution-processing.[41,42] The SEM/EDX analyses for the $r = 0.6$ as-deposited, annealed under BiI_3 vapor, and annealed in N_2 films yield average compositions of $AgBi_{2.01}I_{7.00}$, $Ag_{1.20}Bi_{1.85}I_{7.00}$, and $Ag_{1.12}Bi_{1.04}I_{4.00}$ (the first two close to $AgBi_2I_7$ and the last within experimental uncertainty of $AgBiI_4$), respectively. Considering the error margins for SEM/EDX analysis, these results indicate that annealing in the absence of excess BiI_3 vapor results in the removal of volatile BiI_3 from the film, while maintaining the cubic structure. The average composition of the annealed film under BiI_3 vapor slightly changes from $AgBi_{2.01}I_{7.00}$ to $Ag_{1.20}Bi_{1.85}I_{7.00}$. The annealing process coupled with the still Bi-rich composition (despite the BiI_3 loss during the post-deposition process) may account for the phase transition from the rhombohedral to the cubic structure. Clearly, a change in the film composition (e.g. $AgBi_2I_7$ to $Ag_{1.20}Bi_{1.85}I_{7.00}$ or $AgBiI_4$) upon annealing represents a crucial factor affecting the crystal structure of silver bismuth iodide.[42] In addition, the effect of the cooling process on final crystal structure of the annealed Ag-Bi-I films (180 °C for 15 min under N_2 atmosphere) deposited with $r = 0.6$ was investigated using XRD (**Fig. S2**). For this purpose, the annealed films were either quenched or slow cooled (with an average ~ – 4 °C/min nominal ramp rate) to room temperature. Despite a crystallographic phase transition (from $R\bar{3}m$ to $Fd\bar{3}m$) observed for the post-deposition annealed Ag-Bi-I film ($r = 0.6$; under N_2 and quenched) (**Fig. S1**), the collected XRD pattern of the slow-cooled film (**Fig. S2**) indexes to a rhombohedral unit cell ($R\bar{3}m$). The SEM/EDX analysis for the slow-cooled film yields an average composition of $Ag_{1.30}Bi_{0.90}I_{4.00}$. Apparently, this change in unit cell may be attributed to a slight deviation from the nominal $AgBiI_4$ composition to a more Ag-rich Ag-Bi-I phase, due to further loss of volatile BiI_3 during the slow-cooling process.

As-deposited and post-deposition annealed (180 °C for 15 min under BiI_3 vapor) Ag-rich r = 0.8 films of silver bismuth iodide form in the rhombohedral crystal structure (**Fig. 1c**), with the lattice parameters $a = b$ = 4.3479(1) Å, c = 20.8789(2) Å for the as-deposited film and $a = b$ = 4.3481(1) Å, c = 20.8308(8) Å for the annealed film under BiI_3 vapor. A small trace of AgI impurity was observed for the as-deposited film (**Fig. 1c**), which disappeared after post-deposition annealing under BiI_3 vapor, verifying formation of the final Ag-Bi-I phase via annealing. Note that the estimated lattice parameters for the r = 0.8 annealed film for vacuum-deposited films are consistent with the reported solution-processed Ag_2BiI_5.[48] SEM/EDX measurements show that the as-deposited and annealed films of r = 0.8 have average compositions of $Ag_{1.62}Bi_{1.06}I_{5.00}$ and $Ag_{1.85}Bi_{1.03}I_{5.00}$, respectively, corresponding to (perhaps Ag-poor) Ag_2BiI_5. Further increase in deposition rate ratio to r = 1.2 results in films with AgI impurity peaks in the XRD patterns for both as-deposited and annealed films (**Fig. 1d**) with average compositions of $Ag_{1.96}Bi_{0.95}I_{5.00}$ and $Ag_{1.91}Bi_{0.97}I_{5.00}$, respectively, consistent with the Ag_2BiI_5 composition. The resulting unit cells have rhombohedral structure with $a = b$ = 4.3470(2) Å, c = 20.8617(9) Å for the as-deposited film and $a = b$ = 4.3510(2) Å, c = 20.859(1) Å for the annealed film under BiI_3 vapor.

The Pawley-refined unit cell parameters for the Ag-Bi-I films with different compositions are summarized in **Table S1** along with the corresponding composition of each film obtained from SEM/EDX. Evidently, gradual increase of the AgI content in the coevaporated Ag-Bi-I films (from r = 0.2 to r = 1.2) results in the enlargement of the c lattice constant of the corresponding cells, yielding unit cells with expanded volumes for both rhombohedral and cubic cells. This enlargement of the unit cells presumably originates at least in part from the larger ionic radius of Ag^+ (115 pm) relative to that of Bi^{3+} (103 pm). Existence of vacancies in the crystal structure of Ag-Bi-I permits the wide range of stoichiometries and unit cell size-tunability within the Ag-Bi-I crystals.

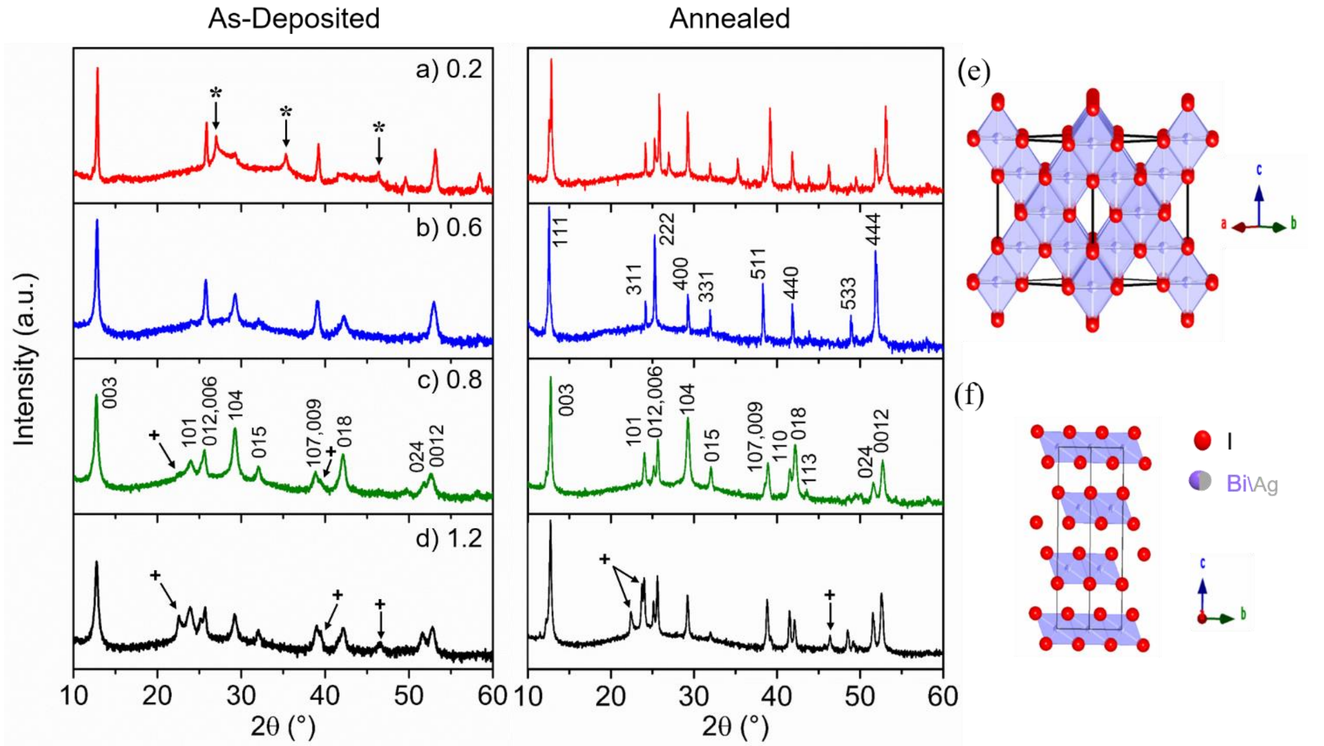

Fig. 1 Experimental XRD patterns for as-deposited (left) and annealed (right) thin films of Ag-Bi-I grown with r = a) 0.2, b) 0.6, c) 0.8, and d) 1.2 rate ratios. All films were annealed at 180 °C for 15 min under BiI_3 vapor, except the as-deposited film of r =

0.2 (180 °C for 15 min in N_2). The as-deposited films index to a rhombohedral structure. Small peaks due to BiI_3 and AgI impurities are marked with "*" and "+", respectively. For *r* = 0.6 and 0.8 annealed films, all peaks index to the known cubic (e) and rhombohedral (f) structure types, respectively. Selected strong diffraction peaks are labeled for each structure type. Unit cell/fitting parameters are listed in Table S1.

TD-XRD measurements were carried out to gain insight into the observed rhombohedral to cubic phase transition mechanism. **Fig. 2** displays the contour plots of the collected XRD patterns from silver bismuth iodide films deposited with a) *r* = 0.6 and c) *r* = 0.8 in the 2θ range from 10°–28°, throughout the annealing and cooling processes under N_2 atmosphere. The temperature profile shown in **Fig. 2b** has three stages: 1) heating from 25 °C to 180 °C with a 50 °C/min ramp rate; 2) hold at 180 °C for 1 hour; 3) cooling to 25 °C with a –10 °C/min nominal ramp rate.

For the as-deposited film with *r* = 0.6, when temperature was elevated from 25 °C to 180 °C, the peaks at 12.84° and 25.82°, assigned to the 003 and 006 reflections of rhombohedral silver bismuth iodide, shift to 12.76° and 25.66°, respectively, due to the thermal expansion of the unit cell (**Fig. 2d**). During the dwell at 180 °C, the diffraction peaks at 12.76°and 25.66° become substantially attenuated, and three other dominant peaks form at 12.5°, 24°, and 25.08°, assigned to 111, 311 and 222 reflections of a cubic silver bismuth iodide structure and indicating the phase transition from the rhombohedral to the cubic structure. The observed lattice constant shift from 180 °C to 25 °C originates from thermal contraction of the resulting unit cell. The cubic phase remains stable, even upon cooling to room temperature (25 °C). The as-deposited and annealed TD-XRD films with *r* = 0.6 exhibit average compositions (as determined by SEM/EDX) of $AgBi_{2.01}I_{7.00}$ and $Ag_{0.77}Bi_{1.10}I_{4.00}$ (**Fig. S5a**), respectively, confirming removal of BiI_3 from the film during the annealing cycle. This observation is consistent with earlier-described results for the annealed film without excess of BiI_3. **Fig. S3** shows no significant difference in the XRD patterns collected over a 6-month period (storage in N_2), indicating high stability of cubic silver bismuth iodide in a nitrogen environment at room temperature.

For the as-deposited film with *r* = 0.8, at 25 °C four dominant diffraction peaks are observed at 12.68°, 23.97°, 25.06°, and 25.55°, characteristic of the rhombohedral crystal structure (**Fig. 2c**). Appearance of two extra rhombohedral diffraction peaks for *r* = 0.8 compared to the as-deposited *r* = 0.6 indicates a higher favorability of randomly-oriented grains for the Ag-rich rhombohedral phase. No phase transition appears during annealing of the thin film, confirming the stability of the rhombohedral phase for deposited silver bismuth iodide films with *r* = 0.8. The observed shifts via heating (25–180 °C) and cooling (180–25 °C) processes originate from thermal expansion and contraction of the unit cell, respectively. Owing to the overlap of the diffraction peaks detected from the as-deposited silver bismuth iodide film (*r* = 0.8) at 25 °C and the annealed film after the cooling process (from 180 to 25 °C) (**Fig. S4**), it can be concluded that the size of the unit cell does not significantly change during annealing, confirming the stability of the stoichiometry of the treated film during TD-XRD. SEM/EDX compositional analysis verifies that the obtained composition for the as-deposited film of *r* = 0.8 ($Ag_{1.62}Bi_{1.06}I_{5.00}$) remains largely unchanged (within the error of the EDX compositional analysis) for the annealed film ($Ag_{1.84}Bi_{1.04}I_{5.00}$) (**Fig. S5b**), presumably because these films already are Bi-poor relative to the films deposited at *r* = 0.6 (which do exhibit a structural change with annealing and a more substantial shift in composition).

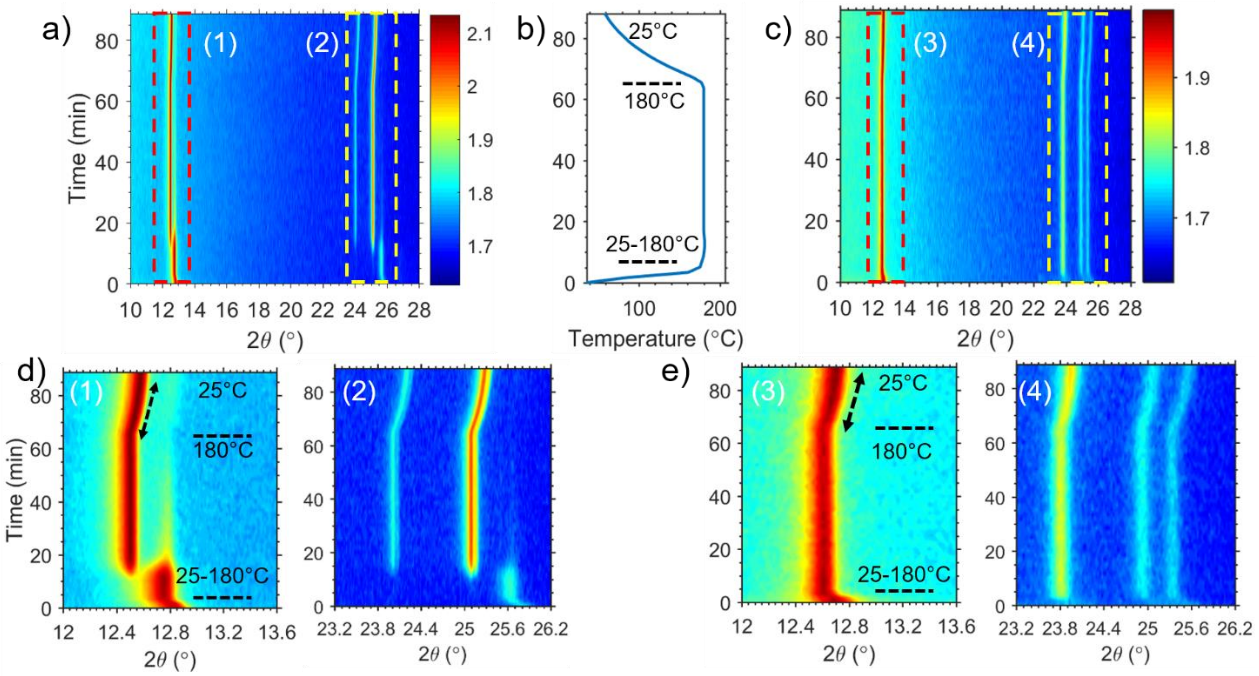

Fig. 2 Evolution of XRD patterns for Ag-Bi-I thin films deposited with a) 0.6 and c) 0.8 rate ratios, during the thermal annealing temperature vs. time profile shown in (b); in a nitrogen atmosphere, the temperature was raised from 25 to 180 °C using a 50 °C/min ramp rate, then held at 180 °C for 1 h, and finally cooled to 25 °C using a -10 °C/min ramp rate. d) 1, 2 and e) 3, 4 show the zoomed areas identified by red and yellow dashed squares in a) and c).

All as-deposited films form primarily within a rhombohedral structure type. From the TD-XRD results, the probability of crystallographic phase transition to the cubic phase upon heating for silver bismuth iodide films is higher for Bi-rich as-deposited film compositions, which might be facilitated by the higher density of vacancies in the $AgBi_2I_7$ crystal structure, enabling vacancy-assisted Ag migration in the crystal via annealing.[33] The phase transition predominantly revolves around a change in the composition from either $AgBi_2I_7$ to $AgBiI_4$, for anneals without BiI_3 vapor followed by a quenching process, or when the Bi-rich silver bismuth iodide film ($AgBi_2I_7$) slightly loses BiI_3 (i.e. $Ag_{1.20}Bi_{1.85}I_{7.00}$) via annealing under BiI_3 vapor. Slight changes in the nominal $AgBiI_4$ composition to either Bi-rich or Ag-rich variants apparently can induce formation of cubic or rhombohedral structures, respectively. On the other hand, increasing Ag-content of the as-deposited films from $AgBi_2I_7$ to Ag_2BiI_5 causes formation of rhombohedral unit cells with a slightly larger c lattice constant. The rhombohedral phase is the more favorable phase for Ag-rich film composition (i.e. near Ag_2BiI_5) at room and elevated temperatures (i.e. 180 °C). Composition is therefore clearly a critical parameter affecting the crystalline phase transition in silver bismuth iodide crystals. Since all compositions, regardless of Ag:Bi ratio, initially form in the rhombohedral form, it appears that temperature and/or thermal annealing can also play a role in the stabilization of the cubic phase. The structural phase transition might therefore additionally follow from an increase in the entropy of the system at elevated temperature. Further studies are needed to fully decipher the detailed nature of the crystallographic phase transitions.

Besides crystal structure analysis, the film grain structure and morphology were investigated using secondary electron SEM imaging. **Fig. 3** shows the surface morphology and associated composition of as-deposited (first row) and post-annealed (second row) coevaporated films with $r = 0.2$ (**Fig. 3a,b**), 0.6 (**Fig. 3c,d**), 0.8 (**Fig. 3e,f**), and 1.2 (**Fig. 3g,h**). All of the deposited films were post-annealed at 180 °C for 15 min under BiI_3 vapor except the as-deposited film with $r = 0.2$ (180 °C for 15 min under N_2). Increasing the annealing temperature above 200 °C results in the evaporation of the volatile BiI_3, leaving yellow AgI on the substrate. For all the deposited films with different rate ratios, the as-deposited films consist of very small grains with average size of 100 nm (first row of **Fig. 3**). Upon annealing, significant grain growth occurs, leading to grains as wide as 3 μm for films with $r = 0.2$ and $r = 0.6$, and 300 nm for $r = 0.8$, with negligible pinhole densities in all the films. As can be seen in **Fig. 3b**, two types of grains grow in the annealed film of $r = 0.2$, indicating (in accordance with the XRD results) the coexistence of multiple phases in the film. Increasing the evaporation rate ratio to 1.2 leads to formation of tiny grains (< 100 nm) and higher pinhole densities (marked by the arrows in **Fig. 3h**). From the obtained film morphologies, it is clear that Bi-rich films help promote formation of large grains via annealing, regardless of whether the film is annealed under BiI_3 vapor ($r = 0.6$) or only under N_2 ($r = 0.2$). SEM/EDX compositional analysis of the grown films in combination with SEM morphological characterization verify that sequential increase in the amount of AgI compared to BiI_3 during the coevaporation process yields the Ag-rich Ag_2BiI_5 phase, promoting the growth of smaller grains via post-deposition annealing under BiI_3 vapor.

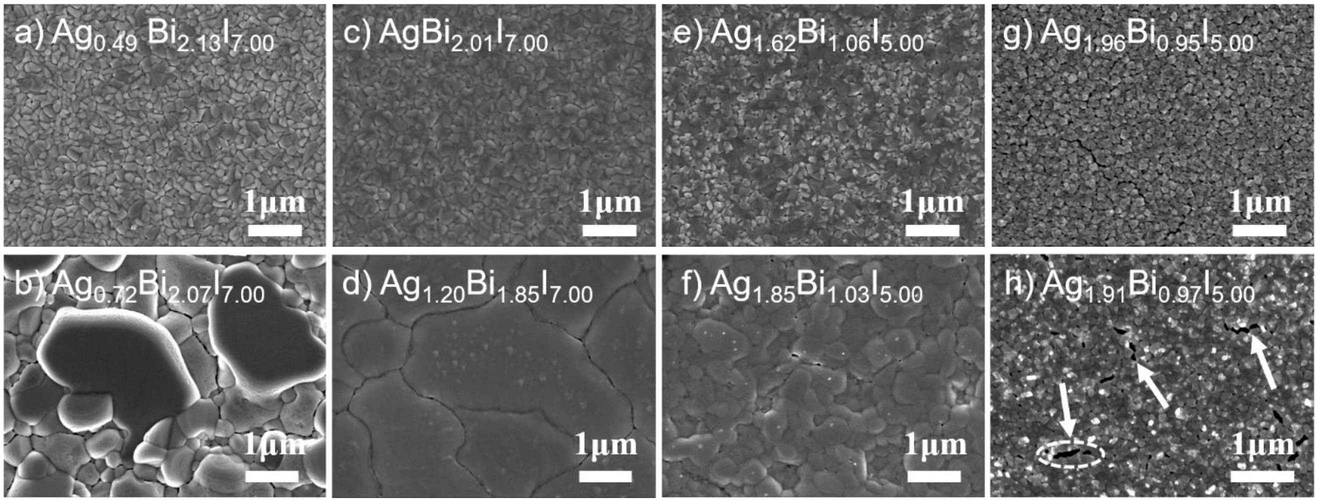

Fig. 3 SEM images of as-deposited (top) and annealed (bottom) films of Ag-Bi-I fabricated with r = (a-b) 0.2, (c-d) 0.6, (e-f) 0.8 and (g-h) 1.2 rate ratios, respectively. Two-step coevaporation/annealing, with annealing at 180 °C for 15 min under BiI_3 vapor (r = 0.6, 0.8 and 1.2) or under N_2 (r = 0.2), was performed to grow the films on glass substrates. Average composition of each film was determined by SEM/EDX and is listed in each panel.

In order to determine the optical band gap of the Ag-Bi-I annealed films with different compositions, the absorption spectra were collected using UV-Vis optical spectroscopy (**Fig. 4a**). Tauc plots were constructed with the assumption of a direct band gap (**Fig. 4b**), leading to the values 1.80 eV, 1.83 eV, and 1.90 eV for $AgBiI_4$, $AgBi_2I_7$, and Ag_2BiI_5 (estimated error = ±0.02), respectively, which correspond well with the previously published values for the solution-based films of $AgBiI_4$,[42,51] $AgBi_2I_7$,[40] and Ag_2BiI_5.[49] The increase in direct band gap energy from $AgBi_2I_7$ to Ag_2BiI_5 may perhaps be rationalized, at least in part, by an increased incorporation of the wide-band-gap AgI into the film structure. Due to uncertainty in the directness or indirectness of the band gaps for these compounds, the indirect band gap values of 1.72 eV, 1.72 eV, and 1.82 eV have also been calculated for $AgBi_2I_7$, $AgBiI_4$, and Ag_2BiI_5 (estimated error = ±0.02), respectively (**Fig. S6**). Photoluminescence (PL) measurements were also performed; however, measured PL intensities were low, suggesting either nominally indirect band gaps or prevalence of defects within the semiconducting films.

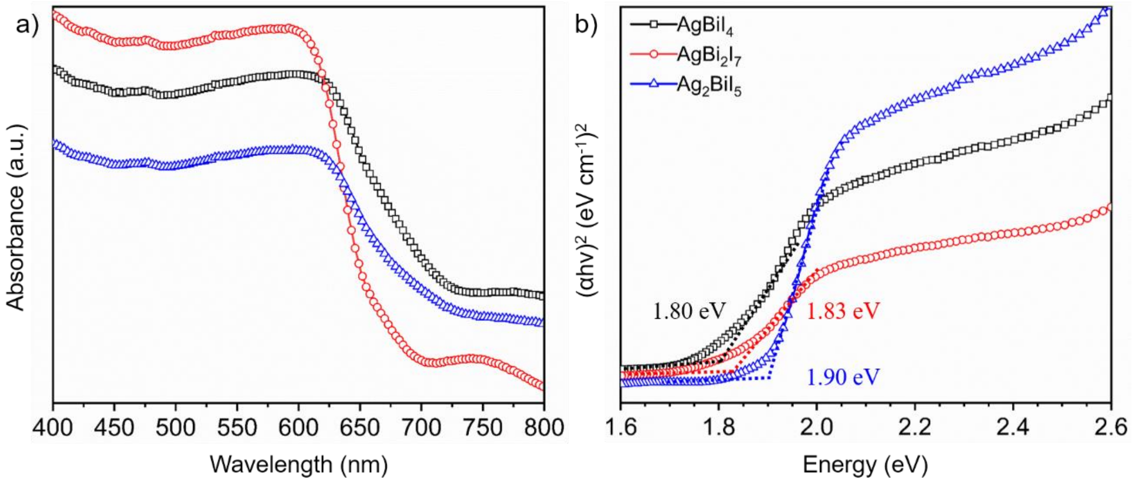

Fig. 4 a) Absorption spectra of $AgBiI_4$, $AgBi_2I_7$ and Ag_2BiI_5 films, deposited using the two-step coevaporation approach on glass substrates and b) Tauc plots of the corresponding films calculated from UV-Vis spectroscopy data assuming direct band gaps.

The electronic structure properties of $AgBi_2I_7$, $AgBiI_4$, and Ag_2BiI_5 were studied using PES measurements on the Ag-Bi-I films with *r* = 0.6 and 0.8. According to our previous study,[53] since sputter cleaning induces detrimental effects on silver bismuth iodide films, the PES study was performed on the as-loaded films. Prior to UPS and IPES measurements, compositional characterization was accomplished using XPS. Apart from presumably adventitious contributions of oxygen (530 eV) and carbon (285 eV), no other contaminants were detected for as-loaded samples (**Fig. S7** and **Table S2**). A close-up of the Ag 3d region demonstrates that the Ag content doubles for post deposition annealed films (under BiI_3 vapor) of *r* = 0.8 compared to *r* = 0.6 (**Fig. S8a**). Moreover, a close-up of the Bi 4f and I 3d regions (**Fig. S8b** and **c**) for these films shows a significant decrease in the Bi content for the film with *r* = 0.8 (Ag_2BiI_5), in addition to reduced I content compared to the film with *r* = 0.6 ($AgBi_2I_7$). The observed trends in the XPS data for the fabricated films (**Table S2**) are consistent with the obtained compositions from EDX analysis. Spectra of Bi 4f for the as-loaded $AgBiI_4$ film reveal that N_2 annealing of the deposited *r* = 0.6 Ag-Bi-I film results in the removal of volatile BiI_3 from the film surface and an increase in the relative concentration of Ag, along with appearance of two small shoulders at binding energies of ~ 162 and 157 eV (**Fig. S8b**) originating from metallic Bi (Bi^0).[53] Sputter-cleaning of the $AgBiI_4$ film for 5 and 10 s leads to more distinguishable shoulders (**Fig. S9**), consistent with our recently published report on $Rb_3Bi_2I_9$.[53] Since no trace of metallic bismuth was realized for the annealed films under BiI_3 vapor ($AgBi_2I_7$ and Ag_2BiI_5), Bi/I deficiency on the surface of the annealed Ag-Bi-I film under N_2 ($AgBiI_4$) might result in the formation of Bi^0 on the surface. In our previous XPS studies on annealed films of BiI_3,[53] $Rb_3Bi_2I_9$,[53] and $Cs_3Sb_2I_9$,[54] traces of metallic bismuth and antimony (Sb^0) were detected, consistent with the most recent report on $(CH_3NH_3)_3Bi_2I_9$ and confirming the susceptibility of annealed Bi- and Sb-based semiconductors to form Bi^0/Sb^0 on the surface.[55]

Fig. 5 shows the UPS and IPES spectra of the as-loaded films corresponding to *r* = 0.6 and 0.8. A close up of the UPS He I secondary electron onsets, and combined valence band and IPES conduction band edges of these films are depicted in **Fig. 5a and c**, respectively. The intersection of tangent line fits to the features of interest and the background determines the positions of the secondary electron onsets (E_{onset}), valence band maxima (VBM) and conduction band minima (CBM) for the fabricated films (**Table 1**).

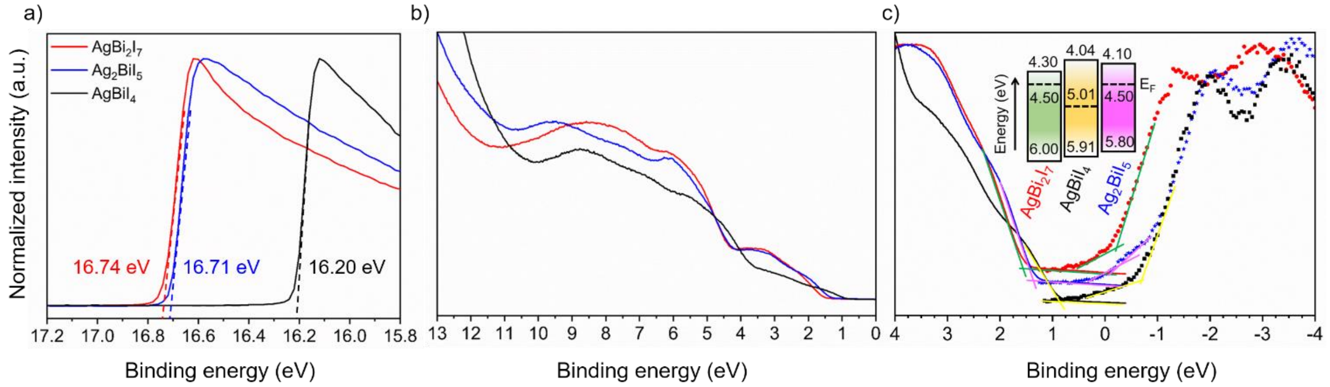

Fig. 5 a) Close up of UPS He I secondary electron onset, b) scan of valence band states, and c) close up of the UPS He I valence band edge and IPES conduction band edge of the as-loaded post-deposition annealed Ag-Bi-I films. Tangent lines are drawn to indicate the onset, valence band edge and conduction band edge locations. The inset gives the band positions for the grown thin films with *r* = 0.6 ($AgBi_2I_7$ and $AgBiI_4$) and *r* = 0.8 (Ag_2BiI_5), derived from UPS and IPES measurements.

Table 1 Derived parameters from UPS and IPES data for the fabricated thin films of $AgBi_2I_7$, $AgBiI_4$, and Ag_2BiI_5. The energy values are referenced to the Fermi level, except for the band gap values.

Fabricated Film	E_{onset} (±0.02) (eV)	E_{VBM} (±0.1) (eV)	IE (±0.1) (eV)	E_{CBM} (±0.3) (eV)	E_g (± 0.3)^a (eV)	$E_g{}^b$ (±0.02) (eV)
$AgBi_2I_7$	16.74	1.50	6.00	−0.20	1.70	1.83
Ag_2BiI_5	16.71	1.30	5.80	−0.40	1.70	1.90
Fabricated Film	E_{onset} (± 0.1) (eV)	E_{VBM} (±0.05) (eV)	IE (± 0.1) (eV)	E_{CBM} (± 0.15) (eV)	E_g (± 0.15)^a (eV)	$E_g{}^b$ (±0.02) (eV)
$AgBiI_4$	16.20	0.90	5.91	−0.97	1.86	1.80

^{a} Calculated from UPS-IPES; ^{b} Calculated from UV-Vis

Based on the obtained UPS results, the ionization energies (IE = hv– (E_{onset}–E_{VBM})) are calculated to be 6.00 eV, 5.91 eV, and 5.80 eV for deposited $AgBi_2I_7$, $AgBiI_4$, and Ag_2BiI_5 films, respectively, with the valence band maxima approximately 1.50 eV, 0.90 eV, and 1.30 eV below the Fermi levels. Furthermore, band gaps (E_g = CBM-VBM) of 1.70 eV and 1.86 eV are derived for $AgBi_2I_7$/Ag_2BiI_5 and $AgBiI_4$ films, respectively. Considering the error margins for the calculation of the conduction band edge, which originate from the slowly varying background in the IPES spectra, the calculated band gaps from UPS/IPES are consistent with the optical band gaps. The estimated band positions for $AgBi_2I_7$ and $AgBi_2I_5$ (**Fig. 5c**, inset) are in good agreement with corresponding values reported for solution-processed films;[40,49] however, to date, no band edge characterization has been reported for solution-based $AgBiI_4$ thin films. From the UPS/IPES data, the fabricated $AgBi_2I_7$ and $AgBi_2I_5$ films are evidently n-type semiconductors, while $AgBiI_4$ is essentially an intrinsic semiconductor.

After characterizing coevaporated silver bismuth iodide film properties, initial photovoltaic devices were prepared using a glass/FTO/TiO_2/$AgBiI_4$/P3HT/Au structure (**Fig. 6a**), in which the $AgBiI_4$ serves as the absorber. For this study, a nominally planar interface between the TiO_2 electron transport layer and $AgBiI_4$ is employed (in contrast to the more typical *mesoporous* interface, used to facilitate charge extraction).[40,43,48-52] Based on the SEM cross-sectional image, the thickness of the $AgBiI_4$ layer is ~ 400 nm, while the thicknesses of TiO_2/P3HT and Au electrode are ~ 20 nm and 70 nm, respectively. The annealed/slow-cooled $AgBiI_4$ film on compact TiO_2 adopts the rhombohedral phase, as determined using XRD analysis (**Fig. S10**). The J-V curves were characterized by a large degree of hysteresis, with PCE measured with a reverse scan (0.89%) falling higher than the PCE measured in the forward scan (0.13%) (**Fig. 6b**). Here, forward and reverse scans refer respectively to sweeping the bias from low to high values, and vice versa. Given the crucial role of interfaces in PV devices,[56-59] the observed hysteresis in this device architecture may originate from a contact barrier or surface-trap defects at the absorber-TiO_2 interface, causing low carrier injection and interfacial recombination centers, respectively. The negligible hysteresis reported for some previous Ag-Bi-I solar cells in the literature might be related to the utilization of the *mesoporous* TiO_2 layer, versus the simpler *planar* TiO_2 in this study.[40,49,50] Further investigation is needed to resolve the role and source of hysteresis, with respect to device performance.

Table 2 lists the characteristic of the device for forward and reverse scan direction. The V_{OC} values are 0.73 V in the forward and 0.84 V in the reverse scan directions, which are among the highest reported V_{OC} values for Ag-Bi-I systems.[40,43,48,49,51] The external quantum efficiency (EQE) spectrum of the $AgBiI_4$ cell (**Fig. 6c**) shows a photocurrent edge below 700 nm (corresponding to ~ 1.77 eV), consistent with the calculated direct band gap from the Tauc plot (1.80 eV). The J_{SC} value (2.39 mA/cm^2) acquired from the integration of the EQE spectrum closely matches the value acquired from the reverse scan J-V curve in **Fig. 6b** (2.37 mA/cm^2). The EQE maximum for this device is 20% at ~ 400 nm. The obtained low EQE, especially at higher wavelengths, is ascribed to considerable charge recombination occurring in the device. A possible factor in the low device performance might be the presence of Bi^0 on the $AgBiI_4$ film surface, as detected during the XPS study. Bi^0 centers could provide recombination sites at the interface between the absorber and the other PV device layers or facilitate Fermi level pinning, thereby degrading device performance.

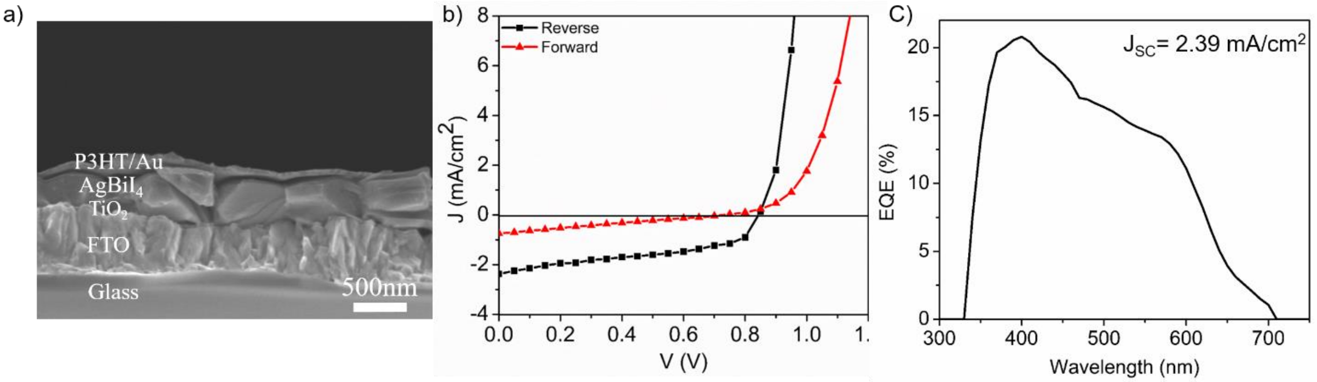

Fig. 6 a) SEM cross-sectional image of the solar cell device employing $AgBiI_4$ absorber layer, compact TiO_2/P3HT as electron/hole transport layers, respectively; b) J-V curves of $AgBiI_4$ solar cell; c) EQE spectrum of $AgBiI_4$ device.

Table 2 Performance parameters for $AgBiI_4$-solar cell with compact TiO_2 as ETL and P3HT as HTL. The cell was measured using forward and reverse scan directions. The integrated J_{SC} from the EQE curve in Fig. 6c is 2.39 mA/cm^2.

Scan direction	V_{OC} (V)	J_{SC} (mA/cm^2)	FF (%)	PCE (%)
Forward	0.73	0.74	23.56	0.13
Reverse	0.84	2.37	44.46	0.89

Conclusions

In summary, we have explored structural, compositional, optical and electrical properties of polycrystalline thin films of semiconducting silver bismuth iodides with general formula $Ag_xBi_yI_z$ ($z = x + 3y$). A versatile two-step approach consisting of coevaporation of metal halides followed by annealing under various atmospheres has been applied for growing smooth and compact films of various Ag-Bi-I stoichiometries and crystal structures. Optimization of the coevaporation and post-deposition annealing processes led to the growth of single-phase cubic $AgBi_2I_7$ and $AgBiI_4$, as well as rhombohedral $AgBiI_4$ and Ag_2BiI_5. TD-XRD in combination with SEM/EDX compositional analysis reveal that, depending on the composition of the as-deposited films and annealing/cooling conditions, a phase transition from rhombohedral to spinel-defect cubic structure can occur. Initial studies on photovoltaic performance of rhombohedral $AgBiI_4$ as light absorber demonstrated a large degree of hysteresis and V_{OC} of as high as 0.84 V and PCE of ~ 0.9% for the reverse scan direction in a planar heterojunction solar cell. Future optimization of planar junction solar cells based on Ag-Bi-I compositions should involve examining the dependence of performance on absorber composition, thickness, as well as device structure.

Conflicts of interest

There are no conflicts to declare.

Author contributions

Maryam Khazaee, Kasra Sardashti and David B. Mitzi devised and directed the project. Maryam Khazaee performed thin film deposition, UV-Vis, SEM, XRD, SEM/EDX, J-V, EQE and analysis of data. Kasra Sardashti assisted in the deposition of thin films. Ching-Chang Chung performed TD XRD measurement. Jon-Paul Sun, Eric Bergmann, and Ian G. Hill performed PES measurements and data analysis. Hanhan Zhou and Jacob L. Jones assisted in SEM/EDX measurements. Maryam Khazaee, Wiley A. Dunlap-Shohl, and Qiwei Han contributed in the solar cell fabrication. Doru C. Lupascu and David B. Mitzi supervised the project.

Acknowledgements

This work was funded in part by the Office of Energy Efficiency and Renewable Energy (EERE), U.S. Department of Energy, under Award Number DE-EE0006712. M.K. and D.C.L. acknowledge financial support through the European Union in the Leitmarktwettbewerb NRW: Neue Werkstoffe, project EFRE-0800120; NW-1-1-040h. I.G.H. acknowledges NSERC CREATE DREAMS and NSERC (RGPIN 298170-2014). J.S. acknowledges Killam Trusts, NSERC and NSERC CREATE DREAMS for financial support. W. A. D.-S. acknowledges support from the Fitzpatrick Institute for Photonics John T. Chambers Scholarship. M.K. and D. B. M. would like to thank C. Mooney for assistance in performing EDX. The work was performed in part at the Duke University Shared Materials Instrumentation Facility (SMIF) and at the Analytical Instrumentation Facility (AIF), members of the North Carolina Research Triangle Nanotechnology Network (RTNN), which is supported by the National Science Foundation (Grant ECCS-1542015) as part of the National Nanotechnology Coordinated Infrastructure (NNCI). All opinions expressed in this paper are the authors' and do not necessarily reflect the policies and views of the DOE or NSF. See the Supporting Information section of this article for more information.

References

1. S. De Wolf, et al., *J. Phys. Chem. Lett.*, 2014, **5**, 1035–1039.

2. N. J. Jeon, et al., *Nature*, 2015, **517**, 476.

3. D. P. McMeekin, et al., *Science*, 2016, **351**, 151–155.

4. C. S. Ponseca Jr, et al., *J. Am. Chem. Soc.*, 2014, **136**, 5189–5192.

5. S. D. Stranks, et al., *Science*, 2013, **342**, 341–344.

6. C. Wehrenfennig, et al., *Adv. Mater.*, 2014, **26**, 1584–1589.

7. G. Xing, et al., *Science*, 2013, **342**, 344–347.

8. M. A. Green, et al., *Nat. Photonics*, 2014, **8**, 506–514.

9. C. Research Cell Efficiency Records; National Center for Photovoltaics at the National Renewable Energy Laboratory: Golden, https://www.nrel.gov/pv/, (accessed December 13, 2018).

10. N. Aristidou, et al., *Angew. Chem. Int. Ed.*, 2015, **54**, 8208–8212.

11. A. Babayigit, et al., *Nat. Mater.*, 2016, **15**, 247–251.

12. M. Bag, et al., *J. Am. Chem. Soc.*, 2015, **137**, 13130–13137.

13. S. N. Habisreutinger, et al., *Nano lett.*, 2014, **14**, 5561–5568.

14. Z. Li, et al., *Chem. Mater.*, 2015, **28**, 284–292.

15. M. Saliba, et al., *Science*, 2016, **354**, 206–209.

16. S. J. Clark, et al., *J. Mater. Chem.*, 1995, **5**, 1813–1818.

17. N. K. Noel, et al., *Energy Environ. Sci.*, 2014, **7**, 3061–3068.

18. B. Saparov, et al., *Chem. Mater.*, 2016, **28**, 2315–2322.

19. C. C. Stoumpos, et al., *J. Am. Chem. Soc*, 2015, **137**, 6804–6819.

20. C. C. Stoumpos, et al., *Inorg. Chem.*, 2013, **52**, 9019–9038.

21. S. Nagane, et al., *J. Phys. Chem. C*, 2018, **122**, 5940-5947.

22. N. Ito, et al., *J. Phys. Chem. Lett.*, 2018, **9**, 1682-1688.

23. X. C. Zeng, et al., US Patent 20180254362, 2018.

24. J.-P. Correa-Baena, et al., *Chem. Mater.*, 2018, **30**, 3734−3742.

25. P. Karuppuswamy, et al., *Nano Energy*, 2018, **45**, 330-336.

26. A. K. Baranwal, et al., *Nano convergence*, 2017, **4**, 26.

27. P. Harikesh, et al., *Chem. Mater.*, 2016, **28**, 7496-7504.

28. F. Jiang, et al., *J. Am. Chem. Soc.*, 2018, **140**, 1019-1027.

29. A. J. Lehner, et al., *Chem. Mater*, 2015, **27**, 7137–7148.

30. K. M. McCall, et al., *Chem. Mater.*, 2017, **29**, 4129–4145.

31. B. W. Park, et al., *Adv. Mater.*, 2015, **27**, 6806–6813.

32. M. Pazoki, et al., *J. Phys. Chem. C*, 2016, **120**, 29039–29046.

33. C. Ran, et al., *J. Phys. Chem. Lett.*, 2017, **8**, 394–400.

34. T. Singh, et al., *ACS Appl. Mater. Interfaces*, 2016, **8**, 14542–14547.

35. S. Sun, et al., *APL Mater.*, 2016, **4**, 031101.

36. K. Du, et al., *Angew. Chem. Int. Ed.*, 2017, **56**, 8158–8162.

37. E. T. McClure, et al., *Chem. Mater.*, 2016, **28**, 1348–1354.

38. B. Zhang, et al., *Sci. China Mater.*, 2018. DOI: 10.1007/s40843-018-9355-0

39. Z. Hu, et al., *ChemSusChem*, 2018, **11**, 2930 – 2935.

40. Y. Kim, et al., *Angew. Chem. Int. Ed.*, 2016, **55**, 9586–9590.

41. T. Oldag, et al., *Z. Anorg. Allg. Chem.*, 2005, **631**, 677–682.

42. H. C. Sansom, et al., *Chem. Mater.*, 2017, **29**, 1538–1549.

43. I. Turkevych, et al., *ChemSusChem*, 2017, **10**, 3754−3759.

44. Z. Xiao, et al., *J. Phys. Chem. Lett.*, 2016, **7**, 3903–3907.

45. K. Dzeranova, et al., *J. Inorg. Chem*, 1985, **30**, 2983–2985.

46. L. F. Mashadieva, et al., *J. Alloys Compd.*, 2013, **551**, 512–520.

47. A. Pisoni, et al., *J. Phys. Chem. Lett.*, 2014, **5**, 2488–2492.

48. H. Zhu, et al., *ChemSusChem*, 2017, **10**, 2592–2596.

49. K. W. Jung, et al., *Sustainable Energy Fuels*, 2018, **2**, 294–302.

50. B. Ghosh, et al., *Adv. Energy Mater.*, 2018, **8**, 1802051.

51. Z. Shao, et al., *Mater. Des.*, 2018, **141**, 81–87.

52. C. Lu, et al., *ACS Appl. Energy Mater.*, 2018, **1**, 4485-4492.

53. M. Khazaee, et al., *Chem. Mater.*, 2018, **30**, 3538–3544.

54. B. Saparov, et al., *Chem. Mater*, 2015, **27**, 5622-5632.

55. S. M. Jain, et al., *Nano Energy*, 2018, **49**, 614–624.

56. S. Weber, et al., *Energy Environ. Sci.*, 2018, DOI: 10.1039/C8EE01447G.

57. H. J. Snaith, et al., *J. Phys. Chem. Lett.*, 2014, **5**, 1511–1515.

58. J. Shi, et al., *Small*, 2015, **11**, 2472–2486.

59. A. Fakharuddin, et al., *Adv. Energy Mater.*, 2017, **7**, 1700623.

Table of Content

Dual-source evaporation approach is applied to deposit $AgBi_2I_7$, $AgBiI_4$ and Ag_2BiI_5 films; a planar junction $AgBiI_4$-solar cell is demonstrated.